Spheroidal-wave analysis of time delay in molecular reconstruction of attosecond beating by interference of two-photon transitions around a Cooper-like minimum

Qinghua Ke,[1] Yueming Zhou,[1,*] Yijie Liao,[1] Min Li,[1] Kunlong Liu,[1] and Peixiang Lu[1,2]

[1]*School of Physics and Wuhan National Laboratory for Optoelectronics, Huazhong University of Science and Technology, Wuhan 430074, China*

[2]*Hubei Key Laboratory of Optical Information and Pattern Recognition, Wuhan Institute of Technology, Wuhan 430205, China*

(Received 17 November 2022; revised 7 March 2023; accepted 14 June 2023; published 19 July 2023)

By numerically solving the three-dimensional time-dependent Schrödinger equation, we have studied the energy- and angle-resolved time delay in H_2^+ photoionization using the reconstruction of attosecond beating by the interference of two-photon transition (RABITT) technique. Around the electron energy of $E_c \sim 1.4$ a.u., the RABITT time delay varies significantly with the energy and emission angle. The time delay changes from positive values to negative values as the increasing energy and emission angle. We have applied the spheroidal wave analysis to reveal this interesting time delay. By analyzing the time-delay dependent modulation of the anisotropic parameters, the energy and angle dependence of the time delay is well interpreted from the perspective of spheroidal wave interference. It shows that the Cooper-like minimum of a p spheroidal wave is responsible for this sign change of the RABITT time delay.

DOI: 10.1103/PhysRevA.108.013112

I. INTRODUCTION

Photoionization of atoms and molecules is one of the most fundamental processes in attosecond science and it can be considered as a half-scattering process where the electron only moves out of the atoms and molecules [1]. The released electron wave function accumulates phase during its escape from atomic and molecular potentials, the energy derivative of which is defined as the Wigner time delay [2–4]. It encodes molecular structure [5,6] and electron dynamics [7,8] information. Measurement of this time delay has attracted increasing interest in the attosecond community. The generation of isolated attosecond pulses [9] and the coherent attosecond pulse train (APT) [10] enabled the attosecond time delay measurement. Using a pump extreme-ultraviolet (XUV) APT assisted by a probe infrared (IR) laser pulse, the reconstruction of attosecond beating by interference of two-photon transition (RABITT) technique has been applied in various noble gases, both theoretically and experimentally [7,8,11–14]. For instance, the time delay difference between the electrons emitted from the 3s and 3p subshell of argon atom has been measured from the angle-integrated photoelectron spectra [7]. The time delay in shake-up ionization has been revealed with RABITT [8]. Moreover, the angle-resolved time delay has been explored with the RABBIT technique [15–25]. By fitting the anisotropy parameters from the momentum distribution of the sidebands, the time delay of different partial waves was successfully extracted [23–26].

In molecules, the complicated structure gives rise to additional interesting phenomena of time delay in photoionization and it has attracted a considerable amount of effort [5,6,27–33]. The attosecond time delays for single-photon ionization of homonuclear and heteronuclear diatomic molecules was presented [28]. Molecular stereo Wigner time delay has also been measured by the orientation- and energy-resolved experiments [5]. Apart from the anisotropic time delay in molecular photoionization, of particular interest is the time delays around shape resonance [32–36] or Cooper minimum, where the time delay changes significantly and it carries electron correlation and internal structure information [31]. With the time-independent R-matrix approach, molecular RABITT time delays of various molecules were calculated and the effects of partial-wave interference and shape resonances were analyzed [32]. The time delay near the shape resonance has been widely measured with the RABBIT technique [33–35], while the time delay around the Cooper minimum has been less explored [37–39]. Recently, time delays between 3s and 3p subshells of argon atom over a large energy range covering the Cooper minima in both subshells was investigated and the sign change of the time delay was observed [39]. The atomic Cooper minimum is attributed to the nodal structure of the radial bound wave function [40]. Regarding photoionization in diatomic molecules, the Cooper-like minimum (CM), which instead owes to the angular bound wave function from the perspective of partial spheroidal waves in the prolate spheroidal coordinate [41,42], occurs more generally. The partial spheroidal waves view of the photoionization is a counterpart picture of the two-center interference as proposed by Cohen and Fano [43,44]. The partial spheroidal wave method has wider applications in diatomic molecule photoionization [45] and nuclear vibrations [46]. Two pictures are consistent at the high-energy regime, where the two-center interference minima correspond to the minima of different partial spheroidal wave cross sections [42]. Recently, the two-center interference induced oscillation of the time delay in

*zhouymhust@hust.edu.cn

a photoionization diatomic molecule has been theoretically predicted [47] and experimentally observed [47,48].

In this work, we applied the partial spheroidal wave analysis of the time delay in molecular RABITT. First, we employed the partial spheroidal wave method to describe the angular distribution in single-photon ionization of H_2^+ at a low-energy region, where the p-spheroidal wave shows the Cooper-like minimum. Then, we studied the energy- and angle-resolved time delay around this minimum using the RABITT technique. The time delay varies abruptly as a function of the photoelectron energy and the emission angle. This energy and angle dependence of the time delay are well interpreted from the point of spheroidal wave interference. Previous studies have focused on the angle-resolved time delay in molecular RABITT, which is attributed to the geometry property of the molecules and qualitatively described by the two-center model [47,48]. With the spheroidal wave method, similar to the partial wave method in atomic photoionization, one is able to describe the angle-resolved time delay in diatomic molecular photoionization where the two-center model fails.

This paper is organized as follows. The numerical methods are given in Sec. II, where we briefly describe the numerical solution of the three-dimensional time-dependent Schrödinger equation (TDSE) and the partial spheroidal wave in the prolate spheroidal coordinate for the diatomic molecule. In Sec. III, we first introduce the spheroidal wave method to explain the angular distributions in single photon ionization. Then, the energy- and angle-resolved time delay around the CM is presented and explained from the perspective of spheroidal wave interference. Conclusions are presented in Sec. IV. Throughout this paper, atomic units (a.u.) are used unless otherwise noted.

II. NUMERICAL METHODS

A. Three-dimensional time-dependent Schrödinger equation

The photoelectron momentum distributions (PEMD) are obtained by numerically solving the three-dimensional TDSE of hydrogen molecule ion H_2^+. It reads

$$i\frac{\partial\psi(\mathbf{r},t)}{\partial t} = H(\mathbf{r},t)\psi(\mathbf{r},t), \tag{1}$$

where the Hamiltonian in velocity gauge within the dipole approximation is

$$H(\mathbf{r},t) = -\tfrac{1}{2}\nabla^2 + V(\mathbf{r};R) - i\mathbf{A}(t)\cdot\overrightarrow{\nabla} \tag{2}$$

and $\overrightarrow{\nabla}$ is the gradient operator. Here $V(\mathbf{r};R)$ is the molecular potential. The nuclei of H_2^+ are fixed at z-axis $z = \pm R/2$ with the internuclear distance $R = 1.4$ a.u. $\mathbf{A}(t) = \hat{z}[A_{\rm IR}(t) + A_{\rm APT}(t)]$ is the total vector potential polarized along the z axis. The vector potential of the IR laser field is

$$A_{\rm IR}(t) = A_i\cos^2\left(\frac{\pi(t-\tau)}{\tau_i}\right)\cos[\omega(t-\tau)], \tag{3}$$

where A_i is the peak amplitude, $\omega = 0.1$ a.u. is the IR frequency, and $\tau_i = 16T$ is the IR pulse duration with $T = 2\pi/\omega$. τ is the time delay between the APT and IR laser pulses ranging from 0 to T separated by $T/40$. The vector potential of APT is represented as the sum of 17 attosecond pulses separated by $T/2$

$$A_{\rm APT}(t) = \sum_{n=-8}^{8} A_n \exp\left[-2\ln 2\left(\frac{t-nT/2}{0.05T}\right)^2\right] \times (-1)^n\cos[N_c\omega(t-nT/2)], \tag{4}$$

where the APT envelope is $A_n = A_a\exp[-2\ln 2(t/4T)^2]$ and $N_c = 29$ is the center harmonic order. The peak intensities of IR and APT pulses are 5×10^{11} and 5×10^{13} W/cm^2, respectively.

The 3D-TDSE in Eq. (1) is solved by the finite-element discrete variable representation method [49] in the spherical coordinate and the details of numerical solution have been given in our previous works [50,51]. The molecular potential $V(\mathbf{r};R)$ for the nuclei-electron interaction is represented by the single-center method [52] and expanded up to maximum angular quantum number $l_{\rm max} = 10$. The maximum box size for the radial coordinate is 80 a.u. and an absorbing mask function is employed with a radius of 30 a.u. At the end of the laser pulse, the wave function propagates under the field-free Hamiltonian for four additional optical cycles of the IR laser pulse to collect the slow electrons. The outer part of the wave function propagates under Volkov Hamiltonian until the end of the laser pulse. The ionization amplitudes are obtained by projecting the outside wave function on the set of scattering states of helium ion He^+ at each time step. The convergence of our calculations has been confirmed by changing the simulation parameters.

B. One-electron two-center problem

To understand to angular distribution of the photoelectron and the energy and emission-angle dependence of the RABITT time delay in the TDSE calculations, we analyze the results in the prolate spheroidal coordinate. For the one-electron two-center Coulomb problem, the Schrödinger equation is written as

$$\left[-\frac{1}{2}\nabla^2 - \frac{Z_1}{r_1} - \frac{Z_2}{r_2}\right]\psi_{\mathbf{k}}(\mathbf{r};R) = E_k\psi_{\mathbf{k}}(\mathbf{r};R), \tag{5}$$

where $E_k = k^2/2$ is the electron energy and r_1 and r_2 are the distances between the electron and two nuclei, respectively. The prolate spheroidal coordinate (ξ,η,ϕ) is introduced as [53]

$$\begin{aligned} \xi &= (r_1+r_2)/R \quad (\xi \geqslant 1),\\ \eta &= (r_1-r_2)/R \quad (-1 \leqslant \eta \leqslant 1),\\ \phi &= \phi \quad (0 \leqslant \phi < 2\pi). \end{aligned} \tag{6}$$

In this coordinate the solutions of Eq. (5) are separable and expressed as [54–57]

$$\psi_{kmq}(\xi,\eta,\phi;R) = X_{mq}(\xi,k)S_{mq}(\eta,k)\frac{\exp(im\phi)}{\sqrt{2\pi}}. \tag{7}$$

Here, m is the magnetic quantum number and q is the angular quantum number, which represents the node number of

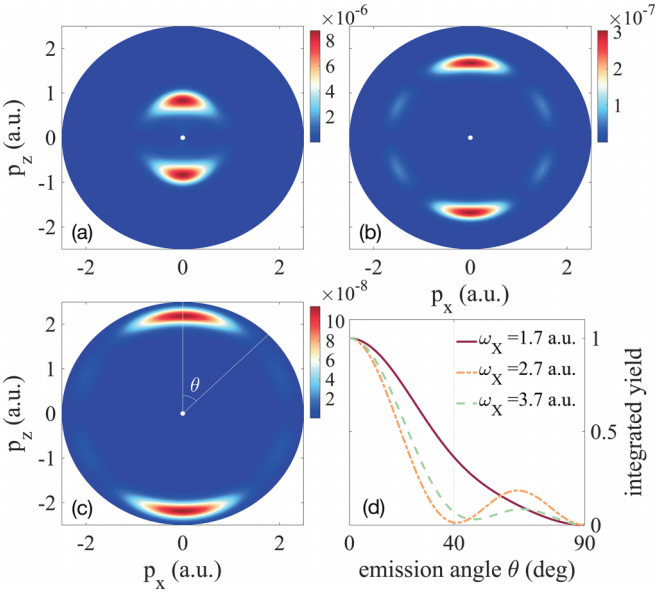

FIG. 1. (a)–(c) PEMDs for single-photon ionization by the XUV laser pulses with the frequencies of 1.7, 2.7, and 3.7 a.u., respectively. (d) The angular distributions of photoelectron with the emission angle ranging from 0° to 90°. The peak laser intensities and the internuclear distance R are fixed at 5×10^{12} W/cm^2 and 1.4 a.u., respectively.

the angular spheroidal functions S_{mq}. The angular and radial Coulomb spheroidal functions follow:

$$\left[\frac{d}{d\eta}(1-\eta^2)\frac{d}{d\eta} + \mathcal{R}_1\eta - c^2\eta^2 - \frac{m^2}{1-\eta^2} + A_{mq}\right]S_{mq} = 0, \tag{8a}$$

$$\left[\frac{d}{d\xi}(\xi^2-1)\frac{d}{d\xi} + \mathcal{R}_2\xi + c^2\xi^2 - \frac{m^2}{\xi^2-1} - A_{mq}\right]X_{mq} = 0, \tag{8b}$$

respectively. Here $\mathcal{R}_1 = R(Z_2 - Z_1)$, $\mathcal{R}_2 = R(Z_2 + Z_1)$, and $c = kR/2$. In our calculations, $Z_1 = Z_2 = 1$ for H_2^+. The separation constant A_{mq} is obtained by the Killingbeck method [58] and then the angular wave functions $S_{mq}(\eta)$ are calculated by the expansion of associated Legendre polynomials (see Appendix 1 for more details) [57]. The radial wave functions $X_{mq}(\xi)$ are solved by means of the direct integration of Eq. (8b) for intermediate values of the variable ξ [57]. The scattering state has the form

$$\Psi_{\mathbf{k}}^{(-)}(\mathbf{r}) = \frac{2\pi}{k}\sum_{m=-\infty}^{\infty}\sum_{q=|m|}^{\infty} i^q e^{-i\Delta_{mq}} S_{mq}(\cos\theta, k) \times X_{mq}(\xi, k) S_{mq}(\eta, k)\frac{\exp[im(\phi-\phi_e)]}{2\pi}, \tag{9}$$

where Δ_{mq} is the scattering phase shift.

III. RESULTS AND DISCUSSIONS

A. Energy dependent angular distribution in single-photon ionization

Figures 1(a)–1(c) show the photoelectron momentum distributions in the polarization plane by single XUV photon ionization with frequency $\omega_X = 1.7$, 2.7, and 3.7 a.u., respectively. For the low-energy case in Fig. 1(a), the PEMD presents two-lobe structure like a p wave. While for the high-energy cases in Figs. 1(b) and 1(c), the PEMDs show the six-lobe structure like an f wave. The corresponding angular distributions (obtained by integrating over the radial momentum) are given in Figs. 1(d). Only the angular distributions with the emission angle ranging from 0° to 90° are shown for symmetry reason. Note that the angular distributions of $\omega_X = 2.7$ (orange dash-dotted line) and 3.7 a.u. (green dashed line) are slightly different. The position of the minimum is located at larger angle for $\omega_X = 3.7$ a.u. Additionally, the photoelectron yield at the minimum for $\omega_X = 2.7$ a.u. approaches zero, while for $\omega_X = 3.7$ a.u. the yield is higher around the minimum.

The angular distributions can be explained from the perspective of partial spheroidal waves. The single-photon transition amplitude is written as

$$M_{\vec{k}}^{(1)} = \langle\Psi_{\mathbf{k}}^{(-)}|\hat{z}|\varphi_0\rangle = \sum_q (-i)^q e^{i\Delta_q} S_q(\hat{k}) T_{Eq}, \tag{10}$$

where T_{Eq} is the partial transition amplitude

$$T_{Eq} = \int \psi_{Eq}(\xi, \eta, \phi)\hat{z}\varphi_0(\xi, \eta, \phi)dV. \tag{11}$$

Here, the volume element is $dV = (\frac{R}{2})^3(\xi^2 - \eta^2)d\xi\, d\eta\, d\phi$ and the dipole operator $\hat{z} = \frac{R}{2}\xi\eta$. The angular and radial parts of ground state φ_0, with the ionization potential $I_p = 1.29$ a.u., are available by the Miller's algorithm [59]. In Eqs. (10) and (11), the index m is neglected for simplicity since the magnetic quantum number is conserved with $m = 0$. The single-photon ionization photoelectron angular distributions are described by $I^{(1)}(k, \theta) \propto |M_{\vec{k}}^{(1)}|^2$.

For the lack of spherical symmetry in molecular potential, more spheroidal waves contribute to the final angular distributions in molecular one-photon photoionization. Due to the up-down symmetry of H_2^+ ground state, only those spheroidal waves of odd parity in Eq. (10) contribute to the final angular distributions. The partial transition amplitudes in Eq. (11) of the lowest odd spheroidal waves ($q = 1, 3, 5$) are presented in Fig. 2(a), where the p and f ($q = 1, 3$) spheroidal waves dominate and the contribution of the higher-order ($q = 5$) spheroidal wave is negligible for the parameters in our calculations. In Fig. 2(a), the transition amplitude of the f-spheroidal wave changes slightly as the photoelectron energy increases, while the transition amplitude of the p-spheroidal wave varies much more rapidly and changes sign at about energy $E_c = 1.45$ a.u., which is similar to the atomic Cooper minimum, mentioned as the Cooper-like minimum (CM). Three vertical dashed lines in Fig. 2(a) indicate the energies corresponding to Figs. 1(a)–1(c), respectively. The angular distribution S_q of the p and f spheroidal waves at these energies are shown in Figs. 2(b) and 2(c). The angular

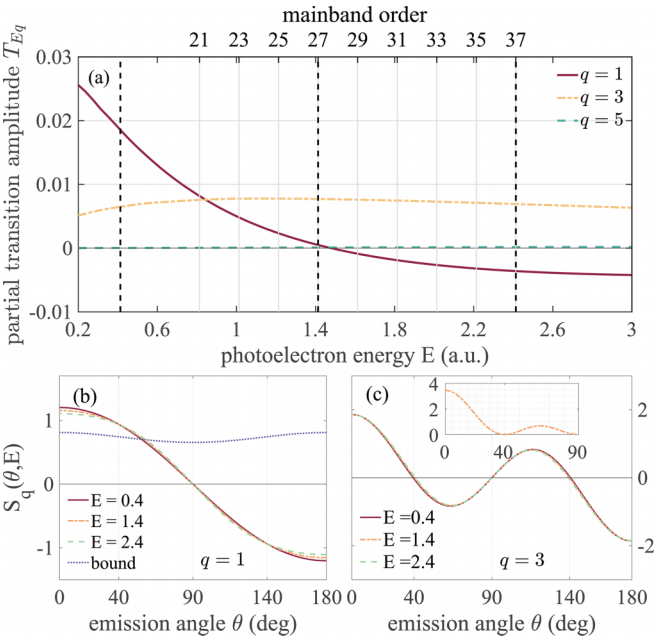

FIG. 2. (a) Partial wave transition amplitudes T_{Eq} as a function of photoelectron energy. The three vertical dashed lines from left to right correspond to the electron energies in Figs. 1(a)–1(c), respectively. The mainband order are also labeled at the top. Figures (b) and (c) are the angular spheroidal function of S_1 and S_3 at $E = 0.4$, 1.4, and 2.4 a.u. The angular part of bound state (dark-blue dashed line) is also shown in (b). The inset in (c) shows the square of S_3 for $E = 1.4$ a.u.

part of the ground state ($q = 0$) is also shown in Fig. 2(b). The inset figure in Fig. 2(c) presents the square of S_3 for $E = 2.4$ a.u.

From Fig. 2(a), the p-spheroidal wave dominates at the low energy in Fig. 1(a). In Fig. 1(b), where the transition amplitude of the p-spheroidal wave is approximately zero and thus only the f-spheroidal wave matters, the angular distribution in Fig. 1(d) shows a minimum around 40°, which is almost the same as the inset figure in Fig. 2(c). At higher energy in Fig. 1(c), the transition amplitude of the f wave is twice as large as that of the p wave. The interference of the p and f partial waves results in the minimum shifting to the value large than 40° and meanwhile the nonzero yield at the minimum, as shown in Fig. 1(d).

B. Time delay in RABITT

In Fig. 3(a), we display the angle-resolved photoelectron spectrum ionized by the APT and IR laser pulses with the time delay $\tau = 0$ and the corresponding angle-integrated photoelectron energy spectrum is presented in Fig. 3(b). The electron absorbs one XUV photon, reaching the mainbands (MB), and subsequently absorbs or emits one IR photon, reaching and interfering at the sidebands (SB). The SB orders are labeled at the right side of Fig. 3(b). The angle-integrated and angle-resolved SB yields exhibit the cosine modulation as a function of the APT/IR time delay τ. Note that the angle-resolved SB yields at each delay τ are obtained by integrating

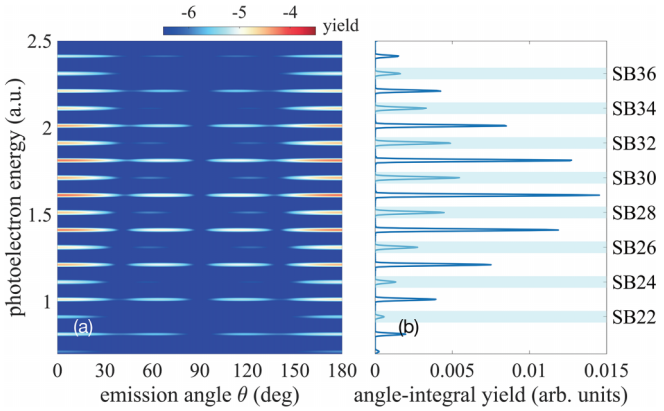

FIG. 3. (a) Angle-resolved PEMD at the APT/IR time delay $\tau = 0$. (b) The angle-integrated photoelectron energy spectrum of (a). The sideband orders are labeled at the right side.

over a small energy range [shadow regions in Fig. 3(b)]. The oscillation of the SB yield as a function of the APT/IR delay τ can be written in general form

$$I(E,\theta,\tau) = A(E,\theta) + B(E,\theta)\cos[2\omega(\tau - \delta\tau)]. \quad (12)$$

By fitting the photoelectron yield at each SB with Eq. (12), the energy- and angle-resolved RABITT time delay $\delta\tau(E,\theta)$ is extracted, as presented in Figs. 4(a) and 4(b). In Fig. 4(a), the energy-resolved time delay is positive at lower energy

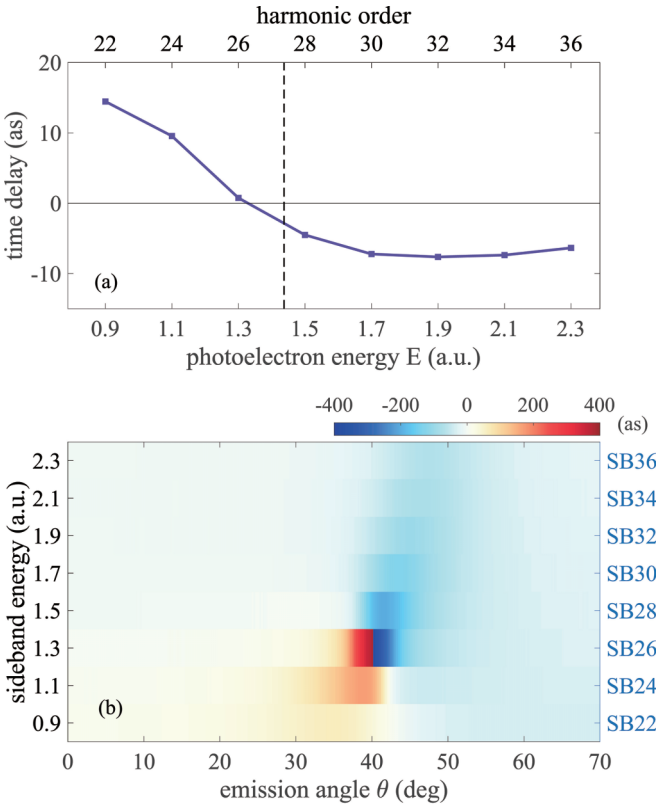

FIG. 4. (a) Angle-integral and (b) angle-resolved RABITT time delay. The vertical dashed line in (a) indicates the CM energy.

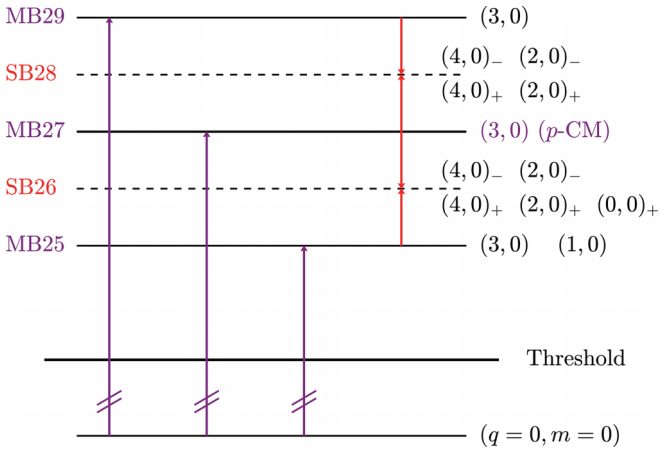

FIG. 5. Photoionization schematic diagram of $H_2{}^+$. Starting from the ground state ($q = m = 0$), the electron absorbs one XUV photon reaching the MBs and subsequently exchanges an IR photon reaching the SBs. The numbers at the right side are the angular and magnetic quantum number (q, m). The positive or negative signs behind represent absorption or emission of an IR photon to reach the SB. The related MB and SB orders are labeled at the left side. The Cooper-like minimum of a p-spheroidal wave locates slightly above MB27.

and turns negative above the CM (indicated by the vertical dashed line). Correspondingly, at the lower orders of SBs in Fig. 4(b), the angle-resolved time delays are positive at small angles and change sign around 40°. At the higher order of SBs, the time delays are negative over the entire angle range. The energy and angle dependence of the RABITT time delay in $H_2{}^+$ photoionization has not been reported in atomic photoionization.

In order to identify the origin of the energy- and angle-resolved RABITT time delay, we present the photoionization schematic diagram around the CM in Fig. 5. Unlike the case in atomic photoionization, there is no strict selection rule for angular quantum number in the transition process, but the dominant channels can be determined by numerical calculations. The magnetic quantum number is conserved for cylindrical symmetry. Starting from the ground state of $H_2{}^+$ ($q = 0, m = 0$), the one-photon channels $(1, 0)$ and/or $(3, 0)$ dominate over the energy range, as indicated in Fig. 2(a). The CM of a p-spheroidal wave occurs at slightly above MB27 and thus only the f-channel (3,0) matters at MB27. At MB29 ($E = 1.6$ a.u.), the transition amplitudes of a p-spheroidal wave are also negligibly small, as shown in Fig. 2(a). For the model molecule and the laser parameters in our calculations, absorption or emission of an IR photon to the SBs changes the angular quantum number by $\Delta q = \pm 1$. Consequently, the SB channels with even angular quantum numbers q up to 4 contribute. The quantum numbers (q, m) of dominant channels at the MBs and SBs around the CM are listed at the right side in Fig. 5. The positive or negative sign beside indicates absorption $(+)$ or emission $(-)$ of one IR photon to reach the SBs, respectively.

Following the notations in atomic perturbation theory [60], the two-photon ionization amplitude in RABBIT can be written as

$$M_{\vec{k}}^{(2\pm)} = \frac{1}{i}\tilde{\mathcal{E}}_{\mathrm{APT}}(\Omega_{\lessgtr})\tilde{\mathcal{E}}_{\mathrm{IR}}(\pm\omega)e^{\pm i\omega\tau}\sum_{q=0,2,4}(-i)^q e^{i\Delta_q}S_q(\hat{k}) \times \lim_{\varepsilon\to 0^+}\sum_{\lambda}\frac{\langle\psi_q|\hat{z}|\psi_\lambda\rangle\langle\psi_\lambda|\hat{z}|\varphi_0\rangle}{\epsilon_0+\Omega_{\lessgtr}-\epsilon_\lambda+i\varepsilon}, = \sum_{q_\pm=0,2,4} e^{\pm i\omega\tau}T_{q_\pm}^{(2\pm)}S_{q_\pm}, \tag{13}$$

where $\Omega_{\lessgtr}$ are the frequencies of the lower or upper order of harmonics and ϵ_0 (ϵ_λ) is the energy of the ground (intermediate) state. $\tilde{\mathcal{E}}_{\mathrm{APT}}$ and $\tilde{\mathcal{E}}_{\mathrm{IR}}$ are the complex amplitudes of the harmonic and IR laser fields in the frequency domain. Therein $T_{q_\pm}^{(2\pm)}$ denotes the two-photon transition matrix of the partial spheroidal wave channels and it can be written as $T_{q_\pm}^{(2\pm)} = |T_{q_\pm}^{(2\pm)}|e^{i\eta_{q_\pm}^{(\pm)}}$ with $q_\pm$ the angular quantum numbers of the absorption or emission channels, respectively. In diatomic molecule photoionization, angular spheroidal functions $S_q(k)$, instead of Legendre polynomials, are adopted to describe the angular distributions. The interference of the spheroidal waves results in the modulation of ionization yield at the SBs,

$$I(E,\theta,\tau) = \left|\sum_{q_+=0,2,4}T_{q_+}^{(2+)}S_{q_+}e^{i\omega\tau} + \sum_{q_-=0,2,4}T_{q_-}^{(2-)}S_{q_-}e^{-i\omega\tau}\right|^2 = A(E,\theta) + 2\left|T_4^{(2+)}\right|^2\mathcal{B}(E,\theta,\tau), \tag{14a}$$

where

$$A(E,\theta) = \left|\sum_{q_+=0,2,4}T_{q_+}^{(2+)}S_{q_+}\right|^2 + \left|\sum_{q_-=0,2,4}T_{q_-}^{(2-)}S_{q_-}\right|^2,$$

and the interference term

$$\begin{aligned}\mathcal{B}(E,\theta,\tau) &= \sum_{q_+=0,2,4}\sum_{q_-=0,2,4}r_{q_+}^{(+)}r_{q_-}^{(-)}f_{q_+,q_-}S_{q_+}S_{q_-}\\ &= r_0^{(+)}r_0^{(-)}f_{0,0}S_0S_0 + r_2^{(+)}r_2^{(-)}f_{2,2}S_2S_2 + r_4^{(-)}f_{4,4}S_4S_4\\ &\quad + [r_0^{(+)}r_2^{(-)}f_{0,2} + r_0^{(-)}r_2^{(+)}f_{2,0}]S_0S_2\\ &\quad + [r_0^{(+)}r_4^{(-)}f_{0,4} + r_0^{(-)}f_{4,0}]S_0S_4\\ &\quad + [r_2^{(+)}r_4^{(-)}f_{2,4} + r_2^{(-)}f_{4,2}]S_2S_4,\end{aligned} \tag{14b}$$

with $f_{q_+,q_-} = \cos[2\omega\tau - \delta\eta_{q_+,q_-})]$, $\delta\eta_{q_+,q_-} = \eta_{q_-}^{(-)} - \eta_{q_+}^{(+)}$, and the positive ratios of the partial transition matrix $r_{q'}^{(\pm)} = |T_{q'}^{(2\pm)}|/|T_4^{(2+)}|$. The product of two angular spheroidal functions $S_{q_+}S_{q_-}$ can be decomposed into a sum of angular spheroidal functions, whose orders mainly range from $|q_+ - q_-|$ to $q_+ + q_-$. From Eq. (14a), the ionization probabilities at the SBs can also be written as

$$I(E_k,\theta,\tau) = \sum_{q'=0,2,4,\ldots}^{q_{\max}}\gamma_{q'}(\tau)S_{q'}(\cos\theta,k), \tag{15}$$

where the real coefficients $\gamma_{q'}$, defined as the anisotropy parameters (AP) [23], quantitatively characterize the angular

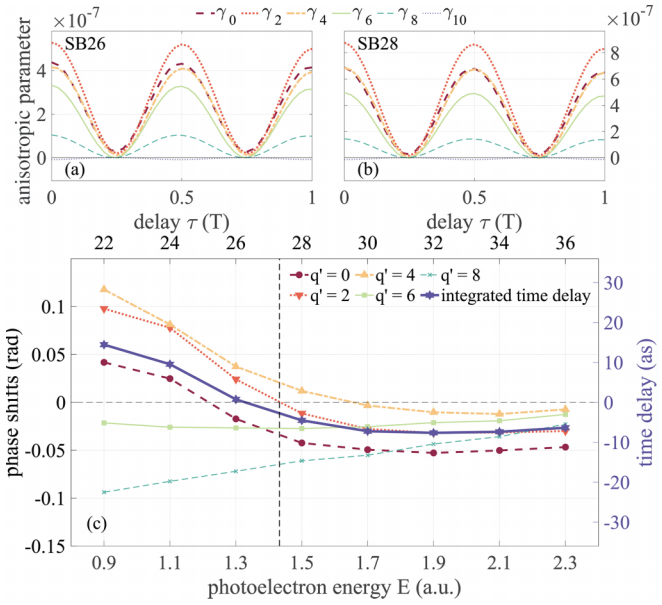

FIG. 6. Anisotropic parameters $\gamma_{q'}$ obtained at (a) SB26 and (b) SB28 as a function of the APT/IR delay τ. (c) The phases $\delta\varphi_{q'}$ extracted from the τ modulations of anisotropic parameters. The angle-integral time delay $\delta\tau_I$ in Fig. 4(a) is also shown in a solid-purple line. The vertical dashed line indicates the CM energy.

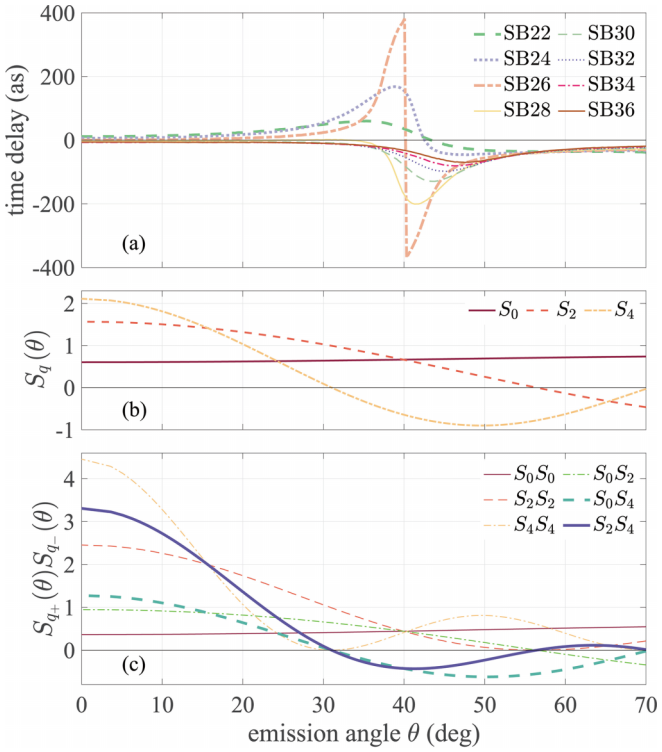

FIG. 7. (a) Same data as Fig. 4(a) but displayed as the curves to show the angular dependence of the RABITT time delay at each SB more clearly. (b) The angular spheroidal functions S_q for $q = 0, 2, 4$ with $E = 1.4$ a.u. (c) The product of two angular spheroidal functions $S_{q_+}S_{q_-}$.

distributions of the SBs and encode the relative contributions of different partial spheroidal waves. The exact expressions of the APs are given in Appendix 2. The APs $\gamma_{q'}(\tau)$ at SB26 and SB28, obtained by projecting the angular distributions at each delay τ to the angular spheroidal functions $S_{q'}$ of order up to $q_{\max} = 10$, are shown in Figs. 6(a) and 6(b). The APs of orders up to $q = 8$ are dominant, while γ_{10} and higher orders are negligibly small. This verifies the two-photon channel analysis in Fig. 4. Moreover, the modulations of different APs exhibit the relative phase shift $\delta\varphi_{q'}$, which is obtained by fitting the AP oscillations using the general form $\gamma_{q'}(\tau) = A_{q'} + B_{q'}\cos(2\omega\tau - \delta\varphi_{q'})$, shown in Fig. 6(c). The vertical dashed black line indicates the p-spheroidal wave CM at $E_c = 1.45$ a.u. The phase shifts $\delta\varphi_{q'}$ of the APs for low orders $q' = 0, 2, 4$ are positive at low energy and become negative at high energy, while those for high orders $q' = 6, 8$ are negative at low energy and increase monotonically over the whole energy range.

According to the orthonormal property of angular spheroidal function for given k, the cross terms in Eq. (14b) with $q_+ \neq q_-$ cancel out after the angle integration and thus the modulations of the angle-integrated yields at SBs have the form

$$\begin{aligned} I_{\rm int}(E,\tau) &= \left|T_4^{(2+)}\right|^2 \sum_{q'=0,2,4} [|r_{q'}^{(+)}|^2 + |r_{q'}^{(-)}|^2 \\ &\quad + 2|r_{q'}^{(+)}||r_{q'}^{(-)}|f_{q',q'}] \\ &= A_{\rm int} + B_{\rm int}\cos[2\omega(\tau - \delta\tau_I)], \end{aligned} \tag{16}$$

where $\delta\tau_I$ is the angle-integral RABITT time delay in Fig. 4(a), presented as the solid-purple line in Fig. 6(c) as well. The angle-integral time delay is positive from SB22 to SB26 and turns negative at higher orders of SBs. From Eq. (16), the angle-integral time delay is determined by the weighted sum of $f_{0,0}$, $f_{2,2}$, and $f_{4,4}$. Notice that the negative phase shift $\delta\varphi_8$ in γ_8 is equal to $\delta\eta_{4,4}$ in $f_{4,4}$, since the highest order of AP has the explicit form $\gamma_8(\tau) \propto |T_4^{(2+)}|^2 + |T_4^{(2-)}|^2 + 2|T_4^{(2+)}||T_4^{(2+)}|f_{4,4}$ (see Appendix 2 for more details), which results from the interference of the absorption and emission channels $(0,0) \to (3,0) \to (4,0)_\pm$. At the SBs below MB27, the interference of the channels $(0,0) \to (1,0) \to (0,0), (2,0)_\pm$ gives rise to positive phase shift $\delta\varphi_{q'}(q' = 0, 2, 4)$, owing to the CM of the p-spheroidal wave. The positive angle-integral time delay at low energy from SB22 to SB26 is attributed to the larger ratio products $|r_{q'}^{(+)}||r_{q'}^{(-)}|(q' = 0, 2)$ than $|r_4^{(-)}|$.

From the perspective of channel competition around the CM, the angle-resolved RABITT time delay in Fig. 4(b) can be also understood. To see more clearly, the angle-resolved time delay is plotted in Fig. 7(a). The time delays at SB22 and SB24 are positive at small angles and turn negative at 43°. Particularly at SB26, the time delay jump occurs at $\theta = 40°$. For higher orders of sidebands, the time delay is always negative. Comparing Eq. (14a) and Eq. (12), we have the relation $2|T_4^{(2+)}|^2\mathcal{B}(E,\theta,\tau) = B(E,\theta)\cos[2\omega(\tau - \delta\tau)]$. The angle-resolved RABITT time delay $\delta\tau$ is determined by the weighted sum of all the $f_{q_+,q_-}S_{q_+}S_{q_-}$ in Eq. (14b). The angular spheroidal functions S_q for $q = 0, 2, 4$ and the products of two spheroidal functions $S_{q_+}S_{q_-}$ are presented in Fig. 7(b) and Fig. 7(c), respectively. In Fig. 7(c), only S_0S_4 and S_2S_4 are negative around $\theta = 40°$. At low energy

$E \approx 1$ a.u., the transition amplitudes of the one-photon ionization channels (1,0) and (3,0) are comparable as shown in Fig. 2(a). For SB22 and SB24, the two-photon channels $(0,0) \to (1,0) \to (0,0)_{\pm}, (2,0)_{\pm}$ with larger transition amplitude ratios dominate over the channels $(0,0) \to (3,0) \to (4,0)_{\pm}$. The interference terms $f_{0,4}$ and $f_{2,4}$ with positive phase shift matter and their corresponding angular spheroidal products S_0S_4 and S_2S_4 in Eq. (14b) change sign over the emission angle, as shown in Fig. 7(c). Hence the time delay at SB22 and SB24 below the CM is positive at small angle and turns negative at large angle. Considering the contribution of other channels, the zero RABITT time delay occurs at larger emission angle 43° than the magic angles of S_4. For SB26 around the CM ($E_c = 1.45$ a.u.), the emission channels $(0,0) \to (1,0) \to (0,0)_{-}, (2,0)_{-}$ are negligible. As a consequence, the interference terms $r_0^{(+)}r_0^{(-)}f_{0,0}$, $r_2^{(+)}r_0^{(-)}f_{2,0}$, and $r_0^{(-)}f_{4,0}$ in Eq. (14b) are negligible and the contributions of the terms $r_0^{(+)}r_2^{(-)}f_{0,2}$, $r_2^{(+)}r_2^{(-)}f_{2,2}$, and $r_2^{(-)}f_{4,2}$ are much reduced. The sum of the remaining oscillation terms $r_0^{(+)}r_4^{(-)}f_{0,4}$, $r_2^{(+)}r_4^{(-)}f_{2,4}$, and $r_4^{(-)}f_{4,4}$ changes sign around the emission angle 40°, where the absolute values of two spheroidal function products are approximately the same. The RABITT time delay jump at SB26 depends on the exact values of the ratios. At higher energy above the CM from SB28 to SB36, the transition amplitude of an f-spheroidal wave is twice as large as that of a p-spheroidal wave in Fig. 2(a). The absorption and emission channels $(0,0) \to (3,0) \to (2,0)_{\pm}, (4,0)_{\pm}$ dominate, the interference of which gives rise to the negative phase shift, including $\delta\varphi_8$ in Fig. 6(c). Because of the suppression of the channels $(0,0) \to (1,0) \to (0,0)_{\pm}, (2,0)_{\pm}$, the interference terms $r_0^{(+)}r_4^{(-)}f_{0,4}$ and $r_2^{(+)}r_4^{(-)}f_{2,4}$ with angular spheroidal function products S_0S_4 and S_2S_4 are suppressed, which is responsible for the sign changes of the angle-resolved RABITT time delay. Thus the weighted sum of rest interference terms is always positive and does not change its sign. As a result, the RABITT time delay for higher order in Fig. 4 is negative over the whole angle range.

IV. CONCLUSIONS

In conclusion, we have studied the RABITT time delay in H_2^+ photoionization around the CM of a p-spheroidal wave. Our single-photon ionization 3D-TDSE results show that the angular photoelectron distribution sensitively depends on the photoelectron energy, which can be understood with spheroidal wave methods. In RABITT, the angle-integral time delay changes from the positive values to the negative values as the photoelectron energy increases. Moreover, there is a sign change in the angle-resolved RABITT time delay at lower orders of SBs for small emission angles, while at higher orders of SBs the time delay is always negative within the angle range. Assisted by the anisotropic parameters, the energy- and angle-resolved RABITT time delay is qualitatively interpreted from the perspective of partial spheroidal wave interference. The two-photon channel competition around the Cooper-like minimum in the p partial spheroidal wave is responsible for this sign change of the RABITT time delay. This work develops the spheroidal wave method in diatomic molecule photoionization, within the philosophy of methods previously implemented in atomic systems. As a counterpart to the two-center interference model, the spheroidal analysis shows the potential in the future study of photoionization at low energy of homo- and heteronuclear diatomic molecules with small internuclear distance.

ACKNOWLEDGMENTS

The authors are grateful to H. Liang and Q. Ning for valuable discussions. This work was supported by the National Key Research and Development Program of China (Grant No. 2019YFA0308300) and the National Natural Science Foundation of China (Grants No. 11874163 and No. 12021004). The computation was completed in the HPC Platform of Huazhong University of Science and Technology.

APPENDIX

1. Solution of the one-electron two-center Coulomb problem

In Sec. II B, we present the solution to the one-electron two-center Coulomb problem. The implemention details are given in this subsection. The solution of Eq. (8a) can be written as an expansion of associated Legendre polynomials [57]

$$S(\eta;k,R) = \sum_{t=m}^{\infty} a_t P_t^m(\eta). \tag{A1}$$

Inserting Eq. (A1) into Eq. (8a), one obtains the five-term recurrence relation of the expansion coefficients a_t,

$$g_1 a_{t+2} + g_2 a_{t+1} + (g_3 + A)a_t + g_4 a_{t-1} + g_5 a_{t-2} = 0, \tag{A2}$$

for $t = m + 2$ and

$$g_1(t) = c^2(t+m+1)(t+m+2)/(2t+3)(2t+5),$$
$$g_2(t) = -\mathcal{R}_1(t+m+1)/(2t+3),$$
$$g_3(t) = t(t+1) + c^2[2t(t+1) - 2m^2 - 1]/(2t-1)(2t+3),$$
$$g_4(t) = -\mathcal{R}_1(t-m)/(2t-1),$$
$$g_5(t) = c^2(t-m-1)(t-m)/(2t-1)(2t-3).$$

The separation constants A can be obtained by the Killingbeck method [58]. In this method, the separation constants and eigenvalues can be calculated from the recurrence relations satisfied by the expansion coefficients. For the continuum states, only the separation constants are unknown. An alternative method is applied to solve the angular part of the continuum state. For given c ($= kR/2$), Eq. (A2) can be written in matrix form

$$\mathbf{g}(t)\mathbf{a} = -A\mathbf{a}, \tag{A3}$$

where $\mathbf{a} = [a_m, a_{m+1}, a_{m+2}, \ldots]^T$. The separation constants A_{mq} and corresponding coefficients vectors $\mathbf{a}_t$ are obtained by directly diagonalizing the five-diagonal coefficient matrix $\mathbf{g}(t)$. Finally, the angular spheroidal functions are normalized so that $\int_{-1}^{1} S^2(\eta;k,R)d\eta = 1$. It is worth noting that $S(\eta)$

tends to associated Legendre polynomial P_t^m ($a_{t=m} = 1$) when c approaches zero.

Once the separation constant A is known, the radial part $X(\xi)$ in Eq. (8b) can be solved to an intermediate value ξ by a variable-step, variable-order Adams-Bashforth-Moulton method. The amplitudes and phase shifts Δ_{mq} of $X(\xi)$ are determined by comparing the intermediate solution and the asymptotic solution [57].

2. Anisotropic parameters

The dominant APs have the forms

$$\begin{aligned}\gamma_0 =& c_0^{(0,0)}\left[\left|T_0^{(2+)}\right|^2 + \left|T_0^{(2-)}\right|^2 + 2\left|T_0^{(2+)}\right|\left|T_0^{(2-)}\right| f_{0,0}\right] \\ &+ c_0^{(2,2)}\left[\left|T_2^{(2+)}\right|^2 + \left|T_2^{(2-)}\right|^2 + 2\left|T_2^{(2+)}\right|\left|T_2^{(2-)}\right| f_{2,2}\right] \\ &+ c_0^{(4,4)}\left[\left|T_4^{(2+)}\right|^2 + \left|T_4^{(2-)}\right|^2 + 2\left|T_4^{(2+)}\right|\left|T_4^{(2+)}\right| f_{4,4}\right],\end{aligned} \tag{A4}$$

$$\begin{aligned}\gamma_2 =& c_2^{(0,2)}\left[\left|T_0^{(2+)}\right|^2 + \left|T_2^{(2-)}\right|^2 + 2\left|T_0^{(2+)}\right|\left|T_2^{(2-)}\right| f_{0,2}\right. \\ &+ \left|T_2^{(2+)}\right|^2 + \left|T_0^{(2-)}\right|^2 + 2\left|T_2^{(2+)}\right|\left|T_0^{(2-)}\right| f_{2,0} \\ &+ T_2^{(2+)}T_0^{(2+)}\cos(\eta_0^{(+)} - \eta_2^{(+)}) \\ &\left.+ T_0^{(2-)}T_2^{(2-)}\cos(\eta_2^{(-)} - \eta_0^{(-)})\right] \\ &+ c_2^{(2,2)}\left[\left|T_2^{(2+)}\right|^2 + \left|T_2^{(2-)}\right|^2 + 2\left|T_2^{(2+)}\right|\left|T_2^{(2-)}\right| f_{2,2}\right] \\ &+ c_2^{(2,4)}\left[\left|T_4^{(2+)}\right|^2 + \left|T_2^{(2-)}\right|^2 + 2\left|T_4^{(2+)}\right|\left|T_2^{(2-)}\right| f_{4,2}\right. \\ &+ \left|T_2^{(2+)}\right|^2 + \left|T_4^{(2-)}\right|^2 + 2\left|T_2^{(2+)}\right|\left|T_4^{(2-)}\right| f_{2,4} \\ &+ T_2^{(2+)}T_4^{(2+)}\cos(\eta_2^{(+)} - \eta_4^{(+)}) \\ &\left.+ T_2^{(2-)}T_4^{(2-)}\cos(\eta_2^{(-)} - \eta_4^{(-)})\right] \\ &+ c_2^{(4,4)}\left[\left|T_4^{(2+)}\right|^2 + \left|T_4^{(2-)}\right|^2 + 2\left|T_4^{(2+)}\right|\left|T_4^{(2+)}\right| f_{4,4}\right],\end{aligned} \tag{A5}$$

$$\begin{aligned}\gamma_4 =& c_4^{(2,2)}\left[\left|T_2^{(2+)}\right|^2 + \left|T_2^{(2-)}\right|^2 + 2\left|T_2^{(2+)}\right|\left|T_2^{(2-)}\right| f_{2,2}\right] \\ &+ c_4^{(0,4)}\left[\left|T_0^{(2+)}\right|^2 + \left|T_4^{(2-)}\right|^2 + 2\left|T_0^{(2+)}\right|\left|T_4^{(2-)}\right| f_{0,4}\right. \\ &+ \left|T_4^{(2+)}\right|^2 + \left|T_0^{(2-)}\right|^2 + 2\left|T_4^{(2+)}\right|\left|T_0^{(2-)}\right| f_{4,0} \\ &+ T_4^{(2+)}T_0^{(2+)}\cos(\eta_0^{(+)} - \eta_4^{(+)}) \\ &\left.+ T_0^{(2-)}T_4^{(2-)}\cos(\eta_4^{(-)} - \eta_0^{(-)})\right] \\ &+ c_4^{(2,4)}\left[\left|T_4^{(2+)}\right|^2 + \left|T_2^{(2-)}\right|^2 + 2\left|T_4^{(2+)}\right|\left|T_2^{(2-)}\right| f_{4,2}\right. \\ &+ \left|T_2^{(2+)}\right|^2 + \left|T_4^{(2-)}\right|^2 + 2\left|T_2^{(2+)}\right|\left|T_4^{(2-)}\right| f_{2,4} \\ &+ T_2^{(2+)}T_4^{(2+)}\cos(\eta_2^{(+)} - \eta_4^{(+)}) \\ &\left.+ T_2^{(2-)}T_4^{(2-)}\cos(\eta_2^{(-)} - \eta_4^{(-)})\right] \\ &+ c_4^{(4,4)}\left[\left|T_4^{(2+)}\right|^2 + \left|T_4^{(2-)}\right|^2 + 2\left|T_4^{(2+)}\right|\left|T_4^{(2+)}\right| f_{4,4}\right],\end{aligned} \tag{A6}$$

$$\begin{aligned}\gamma_6 =& c_6^{(2,4)}\left[\left|T_4^{(2+)}\right|^2 + \left|T_2^{(2-)}\right|^2 + 2\left|T_4^{(2+)}\right|\left|T_2^{(2-)}\right| f_{4,2}\right. \\ &+ \left|T_2^{(2+)}\right|^2 + \left|T_4^{(2-)}\right|^2 + 2\left|T_2^{(2+)}\right|\left|T_4^{(2-)}\right| f_{2,4} \\ &+ T_2^{(2+)}T_4^{(2+)}\cos(\eta_2^{(+)} - \eta_4^{(+)}) \\ &\left.+ T_2^{(2-)}T_4^{(2-)}\cos(\eta_2^{(-)} - \eta_4^{(-)})\right] \\ &+ c_6^{(4,4)}\left[\left|T_4^{(2+)}\right|^2 + \left|T_4^{(2-)}\right|^2 + 2\left|T_4^{(2+)}\right|\left|T_4^{(2+)}\right| f_{4,4}\right],\end{aligned} \tag{A7}$$

$$\gamma_8 = c_8^{(4,4)}\left[\left|T_4^{(2+)}\right|^2 + \left|T_4^{(2-)}\right|^2 + 2\left|T_4^{(2+)}\right|\left|T_4^{(2-)}\right| f_{4,4}\right], \tag{A8}$$

where the momentum-dependent coefficient is

$$c_{q'}^{(q_+,q_-)}(k) = \int_{-1}^{1} S_{q_+} S_{q_-} S_{q'} d\eta. \tag{A9}$$

Here, $c_{q'}$ with q' ranging from $|q_+ - q_-|$ to $q_+ + q_-$ matter and $c_{q'}^{(q_+,q_-)} = c_{q'}^{(q_-,q_+)}$.

[1] J. M. Dahlström, A. L'Huillier, and A. Maquet, Introduction to attosecond delays in photoionization, J. Phys. B: At., Mol., Opt. Phys. **45**, 183001 (2012).

[2] L. Eisenbud, The formal properties of nuclear collisions, Ph.D. thesis, Princeton University, 1948.

[3] E. P. Wigner, Lower limit for the energy derivative of the scattering phase shift, Phys. Rev. **98**, 145 (1955).

[4] F. T. Smith, Lifetime matrix in collision theory, Phys. Rev. **118**, 349 (1960).

[5] J. Vos, L. Cattaneo, S. Patchkovskii, T. Zimmermann, C. Cirelli, M. Lucchini, A. Kheifets, A. S. Landsman, and U. Keller, Orientation-dependent stereo wigner time delay and electron localization in a small molecule, Science **360**, 1326 (2018).

[6] M. Huppert, I. Jordan, D. Baykusheva, A. von Conta, and H. J. Wörner, Attosecond Delays in Molecular Photoionization, Phys. Rev. Lett. **117**, 093001 (2016).

[7] K. Klünder, J. M. Dahlström, M. Gisselbrecht, T. Fordell, M. Swoboda, D. Guénot, P. Johnsson, J. Caillat, J. Mauritsson, A. Maquet, R. Taïeb, and A. L'Huillier, Probing Single-Photon Ionization on the Attosecond Time Scale, Phys. Rev. Lett. **106**, 143002 (2011).

[8] M. Isinger, R. J. Squibb, D. Busto, S. Zhong, A. Harth, D. Kroon, S. Nandi, C. L. Arnold, M. Miranda, J. M. Dahlström, E. Lindroth, R. Feifel, M. Gisselbrecht, and A. L'Huillier, Photoionization in the time and frequency domain, Science **358**, 893 (2017).

[9] M. Schultze, M. Fieß, N. Karpowicz, J. Gagnon, M. Korbman, M. Hofstetter, S. Neppl, A. L. Cavalieri, Y. Komninos, Th. Mercouris, C. A. Nicolaides, R. Pazourek, S. Nagele, J. Feist, J. Burgdörfer, A. M. Azzeer, R. Ernstorfer, R. Kienberger, U. Kleineberg, E. Goulielmakis *et al.*, Delay in photoemission, Science **328**, 1658 (2010).

[10] P. M. Paul, E. S. Toma, P. Breger, G. Mullot, F. Augé, Ph. Balcou, H. G. Muller, and P. Agostini, Observation of a train of attosecond pulses from high harmonic generation, Science **292**, 1689 (2001).

[11] G. Laurent, W. Cao, H. Li, Z. Wang, I. Ben-Itzhak, and C. L. Cocke, Attosecond Control of Orbital Parity Mix Interferences and the Relative Phase of Even and Odd Harmonics in an Attosecond Pulse Train, Phys. Rev. Lett. **109**, 083001 (2012).

[12] A. S. Kheifets, Time delay in valence-shell photoionization of noble-gas atoms, Phys. Rev. A **87**, 063404 (2013).

[13] Á. Jiménez-Galán, L. Argenti, and F. Martín, Modulation of Attosecond Beating in Resonant Two-Photon Ionization, Phys. Rev. Lett. **113**, 263001 (2014).

[14] D. Guénot, D. Kroon, E. Balogh, E. W. Larsen, M. Kotur, M. Miranda, T. Fordell, P. Johnsson, J. Mauritsson, M. Gisselbrecht, K. Varjù, C. L. Arnold, T. Carette, A. S. Kheifets, E. Lindroth, A. L'Huillier, and J. M. Dahlström, Measurements of relative photoemission time delays in noble gas atoms, J. Phys. B: At., Mol., Opt. Phys. **47**, 245602 (2014).

[15] S. A. Aseyev, Y. Ni, L. J. Frasinski, H. G. Muller, and M. J. J. Vrakking, Attosecond Angle-Resolved Photoelectron Spectroscopy, Phys. Rev. Lett. **91**, 223902 (2003).

[16] O. Guyétand, M. Gisselbrecht, A. Huetz, P. Agostini, R. Taïeb, A. Maquet, B. Carré, P. Breger, O. Gobert, D. Garzella, J.-F. Hergott, O. Tcherbakoff, H. Merdji, M. Bougeard, H. Rottke, M. Böttcher, Z. Ansari, and P. Antoine, Evolution of angular distributions in two-colour, few-photon ionization of helium, J. Phys. B: At., Mol., Opt. Phys. **41**, 051002 (2008).

[17] J. Wätzel, A. S. Moskalenko, Y. Pavlyukh, and J. Berakdar, Angular resolved time delay in photoemission, J. Phys. B: At., Mol., Opt. Phys. **48**, 025602 (2015).

[18] S. Heuser, Á. Jiménez Galán, C. Cirelli, C. Marante, M. Sabbar, R. Boge, M. Lucchini, L. Gallmann, I. Ivanov, A. S. Kheifets, J. M. Dahlström, E. Lindroth, L. Argenti, F. Martín, and U. Keller, Angular dependence of photoemission time delay in helium, Phys. Rev. A **94**, 063409 (2016).

[19] I. A. Ivanov and A. S. Kheifets, Angle-dependent time delay in two-color XUV+IR photoemission of He and Ne, Phys. Rev. A **96**, 013408 (2017).

[20] A. W. Bray, F. Naseem, and A. S. Kheifets, Simulation of angular-resolved RABBITT measurements in noble-gas atoms, Phys. Rev. A **97**, 063404 (2018).

[21] C. Cirelli, C. Marante, S. Heuser, C. L. M. Petersson, Á. J. Galán, L. Argenti, S. Zhong, D. Busto, M. Isinger, S. Nandi, S. Maclot, L. Rading, P. Johnsson, M. Gisselbrecht, M. Lucchini, L. Gallmann, J. M. Dahlström, E. Lindroth, A. L'Huillier, F. Martín *et al.*, Anisotropic photoemission time delays close to a Fano resonance, Nat. Commun. **9**, 955 (2018).

[22] S. Donsa, M. Ederer, R. Pazourek, J. Burgdörfer, and I. Březinová, Angle-resolved time delays for shake-up ionization of helium, Phys. Rev. A **102**, 033112 (2020).

[23] J. Fuchs, N. Douguet, S. Donsa, F. Martin, J. Burgdörfer, L. Argenti, L. Cattaneo, and U. Keller, Time delays from one-photon transitions in the continuum, Optica **7**, 154 (2020).

[24] D. You, K. Ueda, E. V. Gryzlova, A. N. Grum-Grzhimailo, M. M. Popova, E. I. Staroselskaya, O. Tugs *et al.*, New Method for Measuring Angle-Resolved Phases in Photoemission, Phys. Rev. X **10**, 031070 (2020).

[25] S. Saha, J. Vinbladh, J. Söngård, A. Ljungdahl, and E. Lindroth, Angular anisotropy parameters for photoionization delays, Phys. Rev. A **104**, 033108 (2021).

[26] W. Jiang, G. S. J. Armstrong, J. Tong, Y. Xu, Z. Zuo, J. Qiang, P. Lu, D. D. A. Clarke, J. Benda, A. Fleischer, H. Ni, K. Ueda, H. W. van der Hart, A. C. Brown, X. Gong, and J. Wu, Atomic partial wave meter by attosecond coincidence metrology, Nat. Commun. **13**, 5072 (2022).

[27] S. Haessler, B. Fabre, J. Higuet, J. Caillat, T. Ruchon, P. Breger, B. Carré, E. Constant, A. Maquet, E. Mével, P. Salières, R. Taïeb, and Y. Mairesse, Phase-resolved attosecond near-threshold photoionization of molecular nitrogen, Phys. Rev. A **80**, 011404 (2009).

[28] P. Hockett, E. Frumker, D. M. Villeneuve, and P. B. Corkum, Time delay in molecular photoionization, J. Phys. B: At., Mol., Opt. Phys. **49**, 095602 (2016).

[29] V. V. Serov and A. S. Kheifets, Angular anisotropy of time delay in XUV+IR photoionization of H_2^+, Phys. Rev. A **93**, 063417 (2016); Time delay in XUV/IR photoionization of H_2O, J. Chem. Phys. **147**, 204303 (2017).

[30] D. Baykusheva and H. J. Wörner, Theory of attosecond delays in molecular photoionization, J. Chem. Phys. **146**, 124306 (2017).

[31] A. Kamalov, A. L. Wang, P. H. Bucksbaum, D. J. Haxton, and J. P. Cryan, Electron correlation effects in attosecond photoionization of CO_2, Phys. Rev. A **102**, 023118 (2020).

[32] J. Benda, Z. Masin, and J. D. Gorfinkiel, Analysis of RABBITT time delays using the stationary multiphoton molecular *R*-matrix approach, Phys. Rev. A **105**, 053101 (2022).

[33] X. Gong, W. Jiang, J. Tong, J. Qiang, P. Lu, H. Ni, R. Lucchese, K. Ueda, and J. Wu, Asymmetric Attosecond Photoionization in Molecular Shape Resonance, Phys. Rev. X **12**, 011002 (2022).

[34] S. Nandi, E. Plésiat, S. Zhong, A. Palacios, D. Busto, M. Isinger, L. Neoričić, C. L. Arnold, R. J. Squibb, R. Feifel, P. Decleva, A. L'Huillier, F. Martín, and M. Gisselbrecht, Attosecond timing of electron emission from a molecular shape resonance, Sci. Adv. **6**, eaba7762 (2020).

[35] S. Heck, D. Baykusheva, M. Han, J.-B. Ji, C. Perry, X. Gong, and H. J. Wörner, Attosecond interferometry of shape resonances in the recoil frame of CF_4, Sci. Adv. **7**, eabj8121 (2021).

[36] H. Ahmadi, E. Plésiat, M. Moioli, F. Frassetto, L. Poletto, P. Decleva, C. D. Schröter, T. Pfeifer, R. Moshammer, A. Palacios, F. Martin, and G. Sansone, Attosecond photoionisation time delays reveal the anisotropy of the molecular potential in the recoil frame, Nat. Commun. **13**, 1242 (2022).

[37] A. Mandal, P. C. Deshmukh, A. S. Kheifets, V. K. Dolmatov, and S. T. Manson, Angle-resolved Wigner time delay in atomic photoionization: The 4*d* subshell of free and confined Xe, Phys. Rev. A **96**, 053407 (2017).

[38] J. Vinbladh, J. M. Dahlström, and E. Lindroth, Many-body calculations of two-photon, two-color matrix elements for attosecond delays, Phys. Rev. A **100**, 043424 (2019).

[39] C. Alexandridi, D. Platzer, L. Barreau, D. Busto, S. Zhong, M. Turconi, L. Neoričić, H. Laurell, C. L. Arnold, A. Borot, J.-F. Hergott, O. Tcherbakoff, M. Lejman, M. Gisselbrecht, E. Lindroth, A. L'Huillier, J. M. Dahlström, and P. Salières, Attosecond photoionization dynamics in the vicinity of the Cooper minima in argon, Phys. Rev. Res. **3**, L012012 (2021).

[40] J. W. Cooper, Photoionization from outer atomic subshells. A model study, Phys. Rev. **128**, 681 (1962).

[41] J. Fernández, O. Fojón, A. Palacios, and F. Martín, Interferences from Fast Electron Emission in Molecular Photoionization, Phys. Rev. Lett. **98**, 043005 (2007).

[42] R. Della Picca, P. D. Fainstein, M. L. Martiarena, and A. Dubois, Zeros in the photoionization partial cross sections of H_2^+, Phys. Rev. A **77**, 022702 (2008); R. Della Picca, P. D. Fainstein, M. L. Martiarena, N. Sisourat, and A. Dubois, Cooper minima and Young-type interferences in photoionization of one-electron molecular ions, *ibid.* **79**, 032702 (2009); R. Della Picca, P. D. Fainstein, and A. Dubois, Cooper minima and Young-type interferences in the photoionization of $H_2{}^+$, *ibid.* **84**, 033405 (2011).

[43] H. D. Cohen and U. Fano, Interference in the photo-ionization of molecules, Phys. Rev. **150**, 30 (1966).

[44] I. G. Kaplan and A. P. Markin, Interference phenomena in photoionization of molecules, Sov. Phys. Dokl. **14**, 36 (1969).

[45] H. Miyagi, T. Morishita, and S. Watanabe, Electron scattering and photoionization of one-electron diatomic molecules, Phys. Rev. A **85**, 022708 (2012).

[46] A. L. Wang, V. V. Serov, A. Kamalov, P. H. Bucksbaum, A. Kheifets, and J. P. Cryan, Role of nuclear-electronic coupling in attosecond photoionization of H_2, Phys. Rev. A **104**, 063119 (2021).

[47] Y. Liao, Y. Zhou, L.-W. Pi, Q. Ke, J. Liang, Y. Zhao, M. Li, and P. Lu, Two-center interference and stereo Wigner time delay in photoionization of asymmetric molecules, Phys. Rev. A **104**, 013110 (2021).

[48] S. Heck, M. Han, D. Jelovina, J.-B. Ji, C. Perry, X. Gong, R. Lucchese, K. Ueda, and H. J. Wörner, Two-Center Interference in the Photoionization Delays of Kr_2, Phys. Rev. Lett. **129**, 133002 (2022).

[49] T. N. Rescigno and C. W. McCurdy, Numerical grid methods for quantum-mechanical scattering problems, Phys. Rev. A **62**, 032706 (2000).

[50] J. Liang, W.-C. Jiang, S. Wang, M. Li, Y. Zhou, and P. Lu, Atomic dynamic interference in intense linearly and circularly polarized XUV pulses, J. Phys. B: At., Mol., Opt. Phys. **53**, 095601 (2020).

[51] Q.-H. Ke, Y.-M. Zhou, Y.-J. Liao, J.-T. Liang, Y. Zhao, J. Tan, M. Li, and P.-X. Lu, Helicity-dependent time delays in multiphoton ionization by two-color circularly polarized laser fields, Front. Phys. **16**, 52503 (2021).

[52] Ph. V. Demekhin, A. Ehresmann, and V. L. Sukhorukov, Single center method: A computational tool for ionization and electronic excitation studies of molecules, J. Chem. Phys. **134**, 024113 (2011).

[53] K. Helfrich and H. Hartmann, Generalized quantum mechanical two-centre problems, Theor. Chim. Acta **16**, 263 (1970).

[54] L. I. Ponomarev and L. N. Somov, The wave functions of continuum for the two-center problem in quantum mechanics, J. Comput. Phys. **20**, 183 (1976).

[55] J. Rankin and W. R. Thorson, Continuum wave functions for the two-center, one-electron system, J. Comput. Phys. **32**, 437 (1979).

[56] M. Hiyama and H. Nakamura, Two-center coulomb functions, Comput. Phys. Commun. **103**, 209 (1997).

[57] G. Hadinger, M. Aubert-Frécon, and G. Hadinger, Continuum wavefunctions for one-electron two-centre molecular ions from the Killingbeck-Miller method, J. Phys. B: At., Mol., Opt. Phys. **29**, 2951 (1996).

[58] G. Hadinger, M. Aubert-Frecon, and G. Hadinger, The killingbeck method for the one-electron two-centre problem, J. Phys. B: At., Mol., Opt. Phys. **22**, 697 (1989).

[59] F. Sattin, A routine to compute the energy and wave function for one-electron two-nuclei molecular systems, Comput. Phys. Commun. **105**, 225 (1997).

[60] J. M. Dahlström, D. Guénot, K. Klünder, M. Gisselbrecht, J. Mauritsson, A. L'Huillier, A. Maquet, and R. Taïeb, Theory of attosecond delays in laser-assisted photoionization, Chem. Phys. **414**, 53 (2013).